Valley-controlled propagation of pseudospin states in bulk metacrystal waveguides

Xiao-Dong Chen, Wei-Min Deng, Jin-Cheng Lu, and Jian-Wen Dong*
School of Physics & State Key Laboratory of Optoelectronic Materials and Technologies, Sun Yat-sen University, Guangzhou 510275, China

(Received 15 August 2017; revised manuscript received 1 February 2018; published 1 May 2018)

Light manipulations such as spin-direction locking propagation, robust transport, quantum teleportation, and reconfigurable electromagnetic pathways have been investigated at the boundaries of photonic systems. Recently by breaking Dirac cones in time-reversal-invariant photonic crystals, valley-pseudospin coupled edge states have been employed to realize selective propagation of light. Here, we realize the controllable propagation of pseudospin states in three-dimensional bulk metacrystal waveguides by valley degree of freedom. Reconfigurable photonic valley Hall effect is achieved for frequency-direction locking propagation in such a way that the propagation path can be tunable precisely by scanning the working frequency. A complete transition diagram is illustrated on the valley-dependent pseudospin states of Dirac-cone-absent photonic bands. A photonic blocker is proposed by cascading two inversion asymmetric metacrystal waveguides in which pseudospin-direction locking propagation exists. In addition, valley-dependent pseudospin bands are also discussed in a realistic metamaterials sample. These results show an alternative way toward molding the pseudospin flow in photonic systems.

DOI: 10.1103/PhysRevB.97.184201

I. INTRODUCTION

By taking advantage of the various degrees of freedom such as frequency [1,2], phase [3,4], polarization [5], and momentum [6], light flow control is of growing scientific and technological importance. Recently, by considering the spin-orbit interaction in time-reversal-invariant photonic systems, the propagation of spin states at photonic boundaries has attracted much attention. The spin-filtered effect and unidirectional transmission of spin states have been demonstrated in different photonic systems such as metasurfaces [7,8], metallic slit [9], photonic crystal waveguides [10,11], and chiral nanophotonic interfaces [12,13]. In the past few years, topology has also been verified as a flexible degree of freedom (DOF) to mold the flow of light, and has provided great potential opportunities in photonics [14–18]. Protected by the bulk-edge correspondence [19], two counterpropagating gapless pseudospin-polarized edge states are found at the interfaces of two topologically distinct time-reversal systems [20–22]. By employing such exotic edge states, robust transport and even the reconfigurable detouring of pseudospin states have been demonstrated at photonic boundaries or domain walls [23–26]. It seems that a well-defined photonic boundary is necessary for the observation of photonic pseudospin propagation. Is it possible to control pseudospin flow in a bulk medium without a photonic boundary?

On the other hand, the valley, which labels the energy extrema of the band structure at momentum space, has been employed to achieve a number of intriguing phenomena such as valley-selective Hall transport and circular dichroism in two-dimensional layered materials [27–30]. Regarding the similarity between electronic systems and classical systems, photonic and sonic counterparts of valley Hall topological insulators have been investigated very recently [31–39]. Valley chirality locked beam splitting and topological transport of edge states were proposed and observed. Although most of the reported valley-controlled behaviors are found in systems where Dirac cones are gapped, the two inequivalent but time-reversal K' and K valleys are ubiquitous in periodic triangular and honeycomb lattices, no matter whether Dirac cones are present or not. It suggests that valley photonics and valley acoustics can not only be explored in systems possessing gapped Dirac cones, but also can be extended to general triangular and honeycomb systems.

In this work, we show valley-controlled propagation of pseudospin states in three-dimensional (3D) bulk metacrystal waveguides without Dirac cones. By breaking the inversion symmetry, we find valley-dependent pseudospin bands and the resultant pseudospin gap due to valley-pseudospin interaction. The variation of the pseudospin bands is shown in the plane of two constitutive parameters of metacrystal waveguides. Reconfigurable photonic valley Hall effect is then demonstrated by shifting the working frequency. Pseudospin-direction locking propagation of pseudospin states is also illustrated, confirming that the pseudospin-filtered feature can be achieved by using the valley DOF. Furthermore, a prototype of a photonic blocker is proposed by cascading two metacrystal waveguides. In addition, valley-dependent pseudospin-split bulk bands are also discussed in a realistic sample constructed by nonresonant and electromagnetic-dual metamaterials between two metal plates. These results show a way toward molding the flow of pseudospin states in photonic structures by using a valley as an alternative binary DOF.

II. PSEUDOSPIN STATES IN METACRYSTAL WAVEGUIDE

Figure 1(a) shows the schematic of a metacrystal waveguide consisting of one metacrystal and two parallel metal plates at $z = 0$ and $z = d_0$ (yellow plane). The unit cell of the

*dongjwen@mail.sysu.edu.cn

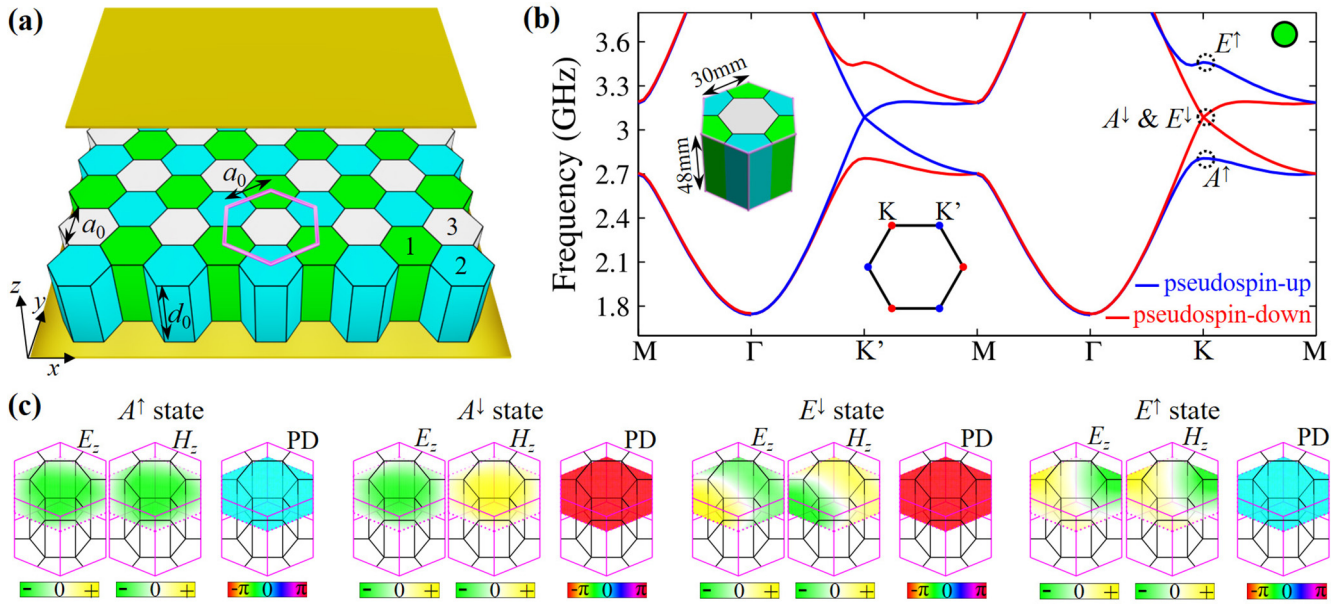

FIG. 1. Valley-dependent pseudospin states in the metacrystal waveguide. (a) Schematic of the inversion asymmetric metacrystal waveguide which is constructed by one electromagnetic-dual metacrystal and two parallel metal plates. The top plate is shifted to reveal the metacrystal inside. The unit cell of the metacrystal has a height of d_0 along the z direction and a hexagonal cross section with the size of a_0 in the xy plane (framed in pink). Each cell is composed of three hexagonal rods which are, respectively, indexed by 1 (green), 2 (cyan), and 3 (gray). (b) Valley-dependent pseudospin bands of the metacrystal waveguide whose feature lengths are $a_0 = 30$ mm and $d_0 = 48$ mm (see the unit cell in the left inset). Three hexagonal rods are set with $\rho = 13$ and $\mu_{\mathbf{r}1} = \mathrm{diag}\{0.455, 0.455, 0.25\}$ [green rod]; $\mu_{\mathbf{r}2} = \mathrm{diag}\{0.67,0.67,0.25\}$ [cyan rod]; $\mu_{\mathbf{r}3} = \mathrm{diag}\{0.39, 0.39, 0.44\}$ [gray rod]. Pseudospin-up and pseudospin-down states are marked in blue and red, respectively. Around the frequency of 3 GHz, pseudospin-down states are prohibited near the K' valley, resulting in a pseudospin-down gap. Similarly, pseudospin-up states are not allowed near the K valley, and this leads to a pseudospin-up gap. The Brillouin zone with high-symmetry K' and K points is shown in the middle inset. (c) Eigenfields of the four lowest pseudospin states at the K point. For each state, the (E_z, H_z) and phase difference (PD) between E_z and H_z at $z = 3d_0/4$ are shown. According to the C_3-rotation eigenvalues of E_z (or H_z) fields, the first and second (third and fourth) states belong to A (E) irreducible representation. Inferring from the phase relation between E_z and H_z (or the resultant PD), the first and fourth states are pseudospin-up polarized while the second and third states are pseudospin-down polarized. As a result, these four states can be respectively labeled as $A^\uparrow$, $A^\downarrow$, $E^\uparrow$, and $E^\downarrow$ states according to the group representations and pseudospin notations [labeling on the eigenfields in (c) and outlined by dashed circles along the band structure in (b)]. Note that the $A^\downarrow$ and $E^\downarrow$ states are accidentally degenerate at the K point by carefully choosing $\mu_{\mathrm{r}1,xx} = 0.455$ [see details in Fig. 2(b)]. This accidental degeneration is different from the structural degeneration of the Dirac point at which two E states are considered.

metacrystal (pink frame) has a hexagonal cross section with a size of a_0 and a height of d_0. Each cell is composed of three hexagonal rods which are indexed by 1 (green), 2 (cyan), and 3 (gray), respectively. For such a metacrystal waveguide, we have the following electromagnetic field solution for the first-order guided modes:

$$\vec{E} = \left[e_x \sin\left(\frac{\pi}{d_0}z\right),\ e_y \sin\left(\frac{\pi}{d_0}z\right),\ -e_z \cos\left(\frac{\pi}{d_0}z\right)\right]^T,\quad \vec{h} = \left[-h_x \cos\left(\frac{\pi}{d_0}z\right),\ -h_y \cos\left(\frac{\pi}{d_0}z\right),\ h_z \sin\left(\frac{\pi}{d_0}z\right)\right]^T, \quad (1)$$

where e_x, e_y, e_z, h_x, h_y, and h_z are functions of (x, y) but the z direction is invariant between $z = 0$ and $z = d_0$. With the definitions of $\vec{e} = (e_x,e_y,e_z)^T$ and $\vec{h} = (h_x,h_y,h_z)^T$, the Maxwell equations can be rewritten in a compact form, yielding

$$\nabla \times \vec{e} = i\omega[\mu_0\mu_{\mathbf{r}}\vec{h} + \xi_{\mathbf{e}}\vec{e}],\quad \nabla \times \vec{h} = -i\omega[\varepsilon_0\varepsilon_{\mathbf{r}}\vec{e} + \xi_{\mathbf{e}}\vec{h}], \quad (2)$$

where $\xi_{\mathbf{e}}$ is an effective bianisotropic tensor with $\xi_{\mathrm{e},xy} = \xi^*_{\mathrm{e},yx} = i\pi/\omega d_0$. Hence, the 3D metacrystal waveguide can be viewed as a two-dimensional (2D) metacrystal with the pseudofields of ($\vec{e}$, $\vec{h}$) and an effective bianisotropic coefficient $\xi_{\mathbf{e}}$ [23]. Note, however, that compared with the electromagnetic fields of ($\vec{E}$, $\vec{H}$) extending infinitely along the z direction in 2D metacrystals (e.g., Ref. [40]), the pseudofields of ($\vec{e}$, $\vec{h}$) are confined between $z = 0$ and $z = d_0$ in 3D metacrystal waveguides. Note also that due to the strong coupling of waveguide modes, the effective bianisotropic coefficient can be large by reducing the height of the waveguide.

In order to construct decoupled pseudospin states, all hexagonal rods are assumed to be uniaxial (i.e., $\mu_{\mathrm{r},xx} = \mu_{\mathrm{r},yy}$) and electromagnetic dual (i.e., $\varepsilon_{\mathbf{r}} = \rho\mu_{\mathbf{r}}$ with ρ being a constant). The electromagnetic-dual symmetry guarantees the occurrence of

photonic Kramer degeneracy [20,40], resulting in the decomposition of the Maxwell equations into two decoupled pseudospins,

$$\nabla \times \begin{pmatrix} p_x^- \\ p_y^- \\ p_z^+ \end{pmatrix} = -i\frac{\omega}{c}\begin{pmatrix} \mu_{\mathrm{r},xx}\sqrt{\rho} & \xi_{\mathrm{e},xy} & \\ \xi_{\mathrm{e},yx} & \mu_{\mathrm{r},xx}\sqrt{\rho} & \\ & & -\mu_{\mathrm{r},zz}\sqrt{\rho} \end{pmatrix}\begin{pmatrix} p_x^- \\ p_y^- \\ p_z^+ \end{pmatrix},$$
$$\nabla \times \begin{pmatrix} p_x^+ \\ p_y^+ \\ p_z^- \end{pmatrix} = i\frac{\omega}{c}\begin{pmatrix} \mu_{\mathrm{r},xx}\sqrt{\rho} & \xi_{\mathrm{e},xy} & \\ \xi_{\mathrm{e},yx} & \mu_{\mathrm{r},xx}\sqrt{\rho} & \\ & & -\mu_{\mathrm{r},zz}\sqrt{\rho} \end{pmatrix}\begin{pmatrix} p_x^+ \\ p_y^+ \\ p_z^- \end{pmatrix}, \tag{3}$$

where $\vec{p}^{\pm} = \sqrt{\rho\varepsilon_0}\vec{e} \pm \sqrt{\mu_0}\vec{h}$. Consequently, for the pseudospin-up states (↑) with nonzero (p_x^-, p_y^-, p_z^+), the in-plane components (e_x,h_x) or (e_y,h_y) are out of phase while the out-of-plane components (e_z, h_z) are in phase [20,41]. On the contrary, for the pseudospin-down states (↓) with nonzero (p_x^+, p_y^+, p_z^-), (e_x, h_x) or (e_y, h_y) are in phase while (e_z, h_z) are out of phase. Although the pseudofields $\vec{e}$ and $\vec{h}$ may not be intuitive, they are closely related to the electromagnetic fields $\vec{E}$ and $\vec{H}$. For example, we write down $\vec{E}$ and $\vec{H}$ at $z = 3d_0/4$ from Eq. (1),

$$\vec{E} = [e_x \sin(3\pi/4),\, e_y \sin(3\pi/4),\;\; e_z \cos(3\pi/4)]^T = [e_x, e_y, e_z]^T/\sqrt{2} \equiv \vec{e}/\sqrt{2},$$
$$\vec{H} = [-h_x \cos(3\pi/4),\;\; -h_y \cos(3\pi/4),\;\; h_z \sin(3\pi/4)]^T = [h_x, h_y, h_z]^T/\sqrt{2} \equiv \vec{h}/\sqrt{2}. \tag{4}$$

It implies that the pseudofields ($\vec{e}$, $\vec{h}$) are linearly proportional to ($\vec{E}$, $\vec{H}$) at $z = 3d_0/4$ in the metacrystal waveguide. As a result, the pseudospin of each state can also be defined by the phase relationship between (E_x,H_x), (E_y,H_y), or (E_z, H_z) at $z = 3d_0/4$. Although the phase relationship between either in-plane or out-of-plane components can be used for pseudospin classification, we focus on the out-of-plane component throughout this paper. That is to say, the pseudospin-up state has in-phase (E_z, H_z) while the pseudospin-down state has out-of-phase (E_z, H_z).

To illustrate the pseudospin classification, we consider a conceptual 3D metacrystal waveguide. The left inset of Fig. 1(b) shows the unit cell of the metacrystal which has a hexagonal cross section with a size of $a_0 = 30$ mm and a height of $d_0 = 48$ mm. In addition, three hexagonal rods are set with $\rho = 13$ and $\mu_{\mathbf{r}1} = \mathrm{diag}\{0.455, 0.455, 0.25\}$; $\mu_{\mathbf{r}2} = \mathrm{diag}\{0.67, 0.67, 0.25\}$; $\mu_{\mathbf{r}3} = \mathrm{diag}\{0.39, 0.39, 0.44\}$ [see more in Sec. III E for the experimental design]. As a result, the electromagnetic-dual symmetry is fulfilled and the pseudospin states are well defined. Figure 1(b) shows the band structure of this inversion-symmetry-breaking metacrystal waveguide. As examples of pseudospin classification, we plot out the eigenfields of four lowest photonic states at the K point in Fig. 1(c), including the E_z, H_z, and their phase difference [(PD), i.e., arg(E_z)–arg(H_z)] at $z = 3d_0/4$. Obviously, the first and fourth lowest states are pseudospin up, as the E_z and H_z are in phase and the resultant PD is 0, while the second and third lowest states are pseudospin down as the PD is π. Thus for the band structure in Fig. 1(b), one can classify all states by marking pseudospin-up (pseudospin-down) states in blue (red). The photonic bands are doubly degenerate along the ΓM direction due to mirror symmetry protection. In contrast, the photonic bands with different pseudospin near K' and K valleys split in the frequency level. Around the frequency of 3 GHz, the pseudospin-down states are prohibited near the K' valley while the pseudospin-up states are prohibited near the K valley. It leads to a valley-dependent pseudospin gap, i.e., frequency range in which pseudospin-up (and equivalently pseudospin-down) states are allowed near one valley but prohibited near the other valley. When such pseudospin gap is frequency isolated, the frequency extrema make the valley an alternative DOF to manipulate the flow of pseudospin states in bulk metacrystal waveguides.

Note that according to the C_3-rotation eigenvalue of E_z (or H_z) fields, the first and second (third and fourth) lowest states at the K point belong to the A (E) irreducible representation [42]. In this way, one can label the four lowest states with different group representations and pseudospin notations, e.g., $A^{\uparrow}$, $A^{\downarrow}$, $E^{\uparrow}$, and $E^{\downarrow}$, as shown in Fig. 1(c). It is distinct from the gapped Dirac cone cases where two $E^{\uparrow}$ and two $E^{\downarrow}$ states should be found, which has been discussed previously, e.g., Ref. [40]. It implies that valley photonics or valley acoustics can be extended to general triangular and honeycomb systems beyond those possessing gapped Dirac cones.

III. RESULTS AND DISCUSSIONS

A. Phase diagram of pseudospin-split bulk states

In this section, we discuss the phase diagram of pseudospin-split bulk states near the K' and K valleys, showing the evolution of pseudospin states. In a time-reversal-invariant system, pseudospin-up and pseudospin-down states are always doubly degenerate when the system is inversion invariant. For example, when rod 1 and rod 2 are of the same constitutive parameters, [i.e., $\mu_{\mathbf{r}1} = \mu_{\mathbf{r}2} = \mathrm{diag}\{0.67, 0.67, 0.25\}$, and see the left inset in Fig. 2(c)], the metacrystal waveguide is inversion symmetric. It results in the doubly degenerate frequency bands in the whole Brillouin zone [Fig. 2(c)]. Such pseudospin degeneracy can be lifted by breaking either time-reversal or inversion symmetry, and we consider the latter case which is more straightforward to realize. To break the inversion symmetry, we keep the constitutive parameters of rod 2 unchanged, but change the constitutive parameters of rod 1 (i.e., $\mu_{\mathrm{r}1,xx}$ and $\mu_{\mathrm{r}1,zz}$). After the inversion symmetry is broken, the pseudospin states near the K' and K valleys will split due to the nonzero valley-pseudospin coupled interaction [40]. Pseudospin states near the K' and K valleys evolve as functions of $\mu_{\mathrm{r}1,xx}$ and $\mu_{\mathrm{r}1,zz}$, and Figure 2(a) shows the phase diagram

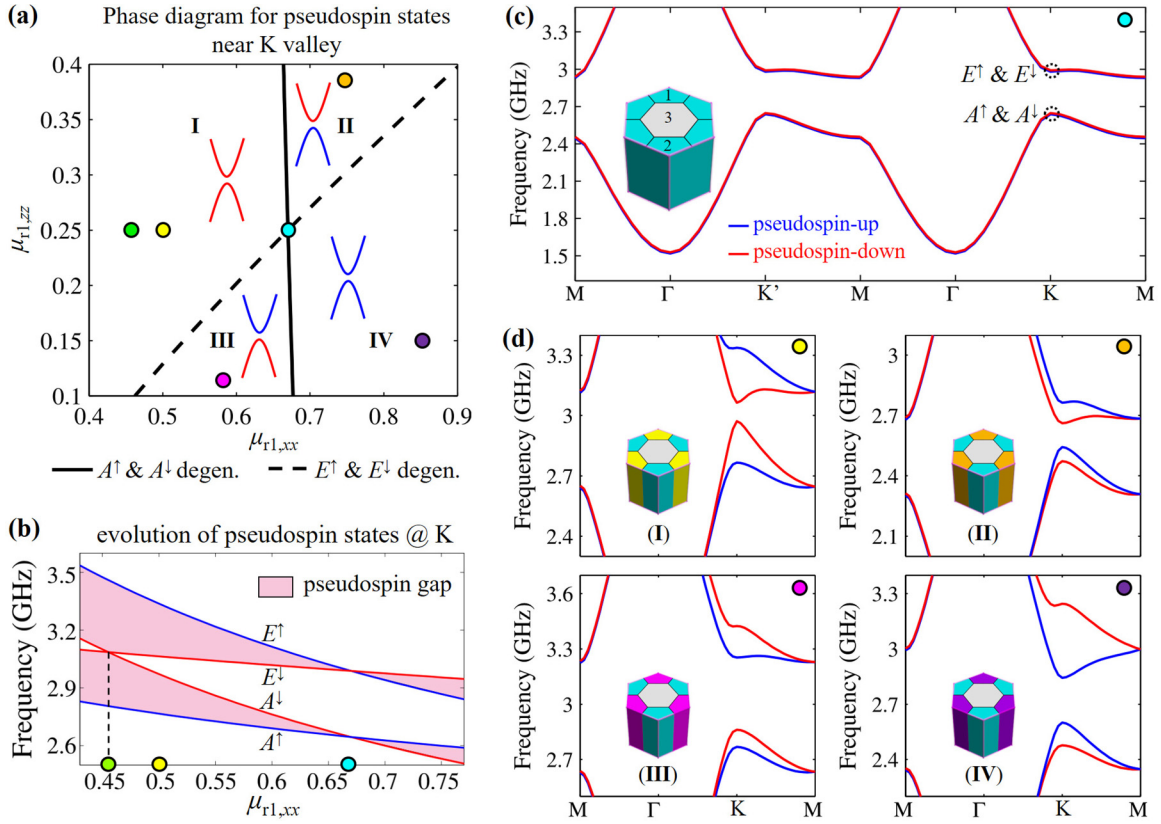

FIG. 2. Variation of pseudospin states near the K valley and band structures of representative metacrystal waveguides. (a) Phase diagram for pseudospin states near the K valley by considering metacrystal waveguides with different $\mu_{r1,xx}$ and $\mu_{r1,zz}$. Here, only the phase diagram and schematics of band structures near the K valley are shown, and those near the K' valley are well predicted according to the time-reversal symmetry. The solid black (dashed black) curve shows the accidental degeneracy between the $A^\uparrow$ and $A^\downarrow$ ($E^\uparrow$ and $E^\downarrow$) states at the K point. These two curves divide the phase diagram into four domains (indexed by Roman numerals from I to IV) which are characterized by different polarizations of the second and third lowest bands near the K valley. (b) Frequency spectra of four pseudospin states at the K point as a function of $\mu_{r1,xx}$, while $\mu_{r1,zz}$ is fixed at 0.25. By achieving the accidental degeneracy between the $A^\downarrow$ and $E^\downarrow$ states, the pseudospin gap bandwidth is maximized at $\mu_{r1,xx} = 0.455$. The green, yellow, and cyan dots are in accordance with those in the phase diagram in (a). (c) Degenerate band structure of the inversion symmetric metacrystal waveguide. The unit cell of metacrystal is shown in the left inset. Three hexagonal rods within the unit cell are marked by indices of 1, 2, and 3, respectively. Rod 1 and rod 2 are set as $\mu_{\mathbf{r}1} = \mu_{\mathbf{r}2} = \text{diag}\{0.67, 0.67, 0.25\}$ while rod 3 is $\mu_{\mathbf{r}3} = \text{diag}\{0.39, 0.39, 0.44\}$. (d) Band structures of four representative metacrystal waveguides in each domain, i.e., metacrystal waveguide with $\mu_{r1,xx} = 0.5$ and $\mu_{r1,zz} = 0.25$ (marked by the yellow dot in domain I), with $\mu_{r1,xx} = 0.74$ and $\mu_{r1,zz} = 0.38$ (marked by the orange dot in domain II), with $\mu_{r1,xx} = 0.58$ and $\mu_{r1,zz} = 0.12$ (marked by the pink dot in domain III), and with $\mu_{r1,xx} = 0.85$ and $\mu_{r1,zz} = 0.15$ (marked by the purple dot in domain IV).

of pseudospin states near the K valley. Note that those near the K' valley can be predicted from the principle of time-reversal symmetry.

In Fig. 2(a), the solid black curve shows the accidental degeneracy between the $A^\uparrow$ and $A^\downarrow$ states at the K point. On the other hand, the dashed black curve shows the accidental degeneracy between the $E^\uparrow$ and $E^\downarrow$ states at the K point. These two curves divide the phase diagram into four domains which are indexed by Roman numerals from I to IV. In each domain, we plot the schematics of the second and third lowest bands near the K valley. For example, in domain I, both the second and third lowest bands are of pseudospin-down polarization [see the two red bands in Fig. 2(a)]. Hence pseudospin-up states are prohibited near the K valley and this leads to a pseudospin-up gap. One representative metacrystal waveguide with $\mu_{r1,xx} = 0.5$ and $\mu_{r1,zz} = 0.25$ in domain I is marked by the yellow dot in Fig. 2(a) and its band structure is shown in the top-left panel of Fig. 2(d). The numerical result proves once again that the second and third lowest bands near the K valley are pseudospin-down polarized. The polarization of these two bands can be changed by altering $\mu_{r1,xx}$ and $\mu_{r1,zz}$, reaching other domains in Fig. 2(a). For example, we consider the metacrystal waveguide with $\mu_{r1,xx} = 0.74$ and $\mu_{r1,zz} = 0.38$ [marked by the orange dot in Fig. 2(a)]. When it goes from the yellow dot to the orange dot in the phase diagram, it passes through the solid black curve, but not the dashed black curve. This implies that there is a mode exchange between the $A^\uparrow$ and $A^\downarrow$ states, but no exchange between the $E^\uparrow$ and $E^\downarrow$ states. Hence for metacrystal waveguides in domain II, the second lowest band changes to be pseudospin-up polarized while the third lowest band stays as pseudospin-down polarized [blue band on the bottom, and red band on the top in domain II in Fig. 2(a)]. This is in good agreement with the calculated band structure given in the top-right panel of Fig. 2(d). On the other

hand, when the metacrystal waveguide goes from domain II to domain IV in the phase diagram, it passes through the dashed black curve. The mode exchange between the $E^{\uparrow}$ and $E^{\downarrow}$ states happens and the third lowest band changes to be pseudospin-up polarized. As a result, both the second and third bands near the K valley become pseudospin-up polarized [see the two blue bands in domain IV in Fig. 2(a)]. This is confirmed by the band structure shown in the lower-right panel of Fig. 2(d) for the metacrystal waveguide with $\mu_{\mathrm{r1},xx} = 0.85$ and $\mu_{\mathrm{r1},zz} = 0.15$ (marked by the purple dot). Lastly in domain III, we consider the metacrystal waveguide with $\mu_{\mathrm{r1},xx} = 0.58$ and $\mu_{\mathrm{r1},zz} = 0.12$ (marked by the pink dot). Its band structure is plotted in the lower-left panel of Fig. 2(d). The second lowest band near the K valley is of pseudospin-down polarization, which is different from that of the purple metacrystal waveguide in domain IV. This is because it experiences a mode exchange between the $A^{\uparrow}$ and $A^{\downarrow}$ states when transforming from domain IV to domain III. In the phase diagram in Fig. 2(a), four different combinations of the polarizations of the second and third bands near the K valley can be found. This indicates a potential way to control pseudospin flow by manipulating the polarizations of pseudospin states and pseudospin gaps (e.g., reconfigurable photonic valley Hall effect presented in Sec. III B).

The bandwidth of the pseudospin gap can be enlarged by the accidental degeneracy between the second and third pseudospin states at the K point (or equivalently the K' point). As an example to achieve such accidental case, we keep $\mu_{\mathrm{r1},zz} = 0.25$ but alter $\mu_{\mathrm{r1},xx}$. Figure 2(b) shows the frequency spectra of four pseudospin states at the K point as a function of $\mu_{\mathrm{r1},xx}$. One can see that the frequencies of these four K valley states increase with the decreasing of $\mu_{\mathrm{r1},xx}$. When $\mu_{\mathrm{r1},xx} = 0.67$ at the cyan dot, the $A^{\uparrow}$ ($E^{\uparrow}$) state superposes to the $A^{\downarrow}$ ($E^{\downarrow}$) state due to the inversion invariance [Fig. 2(c)]. It is interesting to find that two pseudospin-down states (i.e., $A^{\downarrow}$ and $E^{\downarrow}$ states) are accidentally degenerate at $\mu_{\mathrm{r1},xx} = 0.455$ (marked by the green dot). This leads to a pseudospin gap with a 12% gap-midgap ratio [Fig. 1(b)], enabling the broadband pseudospin-flow control.

B. Reconfigurable photonic valley Hall effect

One of the characteristic manifestations of valley-controlled propagation of pseudospin states is the photonic valley Hall effect (PVHE) in which pseudospin states at different valleys can be separately routed. Employing the opposite group velocities of pseudospin states in the second and third bands, reconfigurable PVHE can be achieved by shifting the working frequency. To see this, we consider the metacrystal waveguide in domain IV, e.g., that marked by the purple dot in the phase diagram [Figs. 2 and 3(a)]. As presented in the lower-right panel in Fig. 2(d), the second and third bands near the K valley are pseudospin-up polarized, while those near the K' valley are of pseudospin-down polarization. Two pseudospin gaps, i.e., one ranging from 2.48 to 2.6 GHz and the other from 2.85 to 3 GHz, are found. To determine the propagation directions of pseudospin states in these two gaps, equifrequency contours should be considered. As examples, Figs. 3(b) and 3(c) show the equifrequency contours at the frequency of 2.48 GHz in the second band and the frequency of 2.92 GHz in the third band, respectively. These two contours are similar, but the

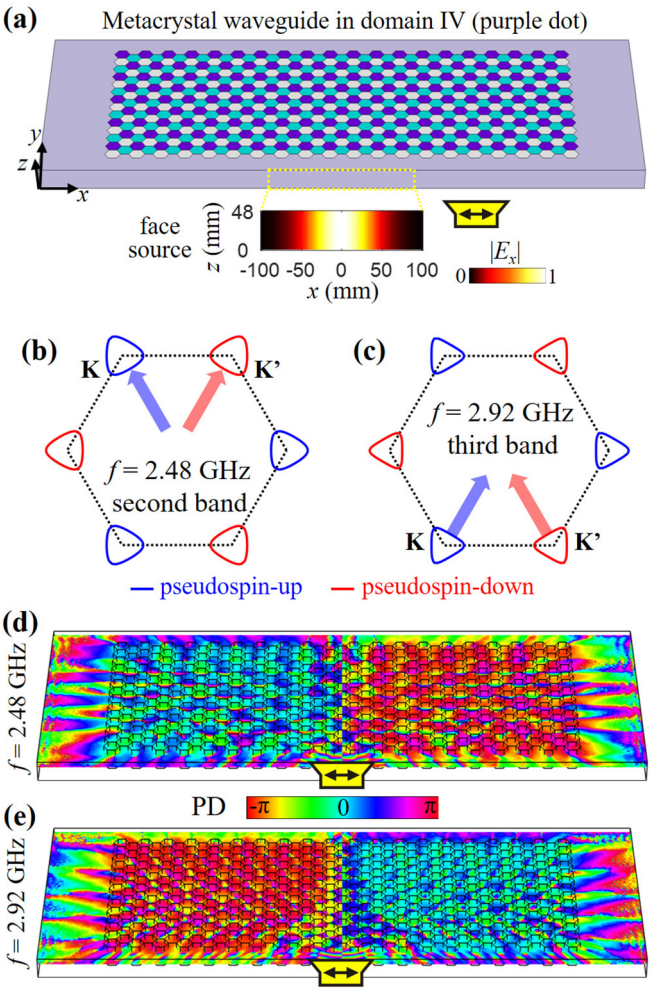

FIG. 3. Reconfigurable photonic valley Hall effect in bulk metacrystal waveguides. (a) Schematic of the metacrystal waveguide in domain IV of Fig. 2(a). Outer light-purple region is the homogeneous dielectric medium with $\varepsilon = 13$ for guiding pseudospin states with matched impedance. The horn-shaped polygon stands for the E_x-polarized face source incident along the $+y$ direction. The face source is homogeneous along the z direction, while it has a Gaussian width of 100 mm along the x direction. (b), (c) Equifrequency contour at the frequency of (b) 2.48 GHz and (c) 2.92 GHz. Pseudospin-up states at these two frequencies have similar contours but different increasing frequency directions, resulting in opposite group velocities (marked by blue arrows). Opposite group velocities are also found in pseudospin-down states (marked by red arrows). This leads to the frequency-direction locking pseudospin flow, i.e., reconfigurable photonic valley Hall effect (PVHE). (d), (e) The PD distributions when the incident source is operated at the frequency of (d) $f = 2.48$ GHz, and (e) $f = 2.92$ GHz. In (d), pseudospin-up states propagate along the ΓK direction while pseudospin-down states propagate along the $\Gamma K'$ direction. However, in (e), the pseudospin-flow directions are reversed, and hence reconfigurable PVHE is confirmed.

pseudospin states on them propagate along opposite directions. For example, pseudospin-up states with $f = 2.48$ GHz propagate along the ΓK direction [blue arrow in Fig. 3(b)], while they switch to propagate along the $\Gamma K'$ direction when the frequency of 2.92 GHz is considered [blue arrow in Fig. 3(c)]. This is because the propagation direction of the pseudospin

state, i.e., the group velocity, is perpendicular to the contour and points in the direction of increasing frequency. For the second band, the direction of increasing frequency points toward the valley center, while it points away from the valley center for the third band. With these opposite group velocities, reconfigurable PVHE is expected [Figs. 3(d) and 3(e)]. To see this, an E_x-polarized face source, which is homogeneous along the z direction and has a Gaussian width of 100 mm along the x direction, is launched into the metacrystal waveguide along the $+y$ direction [marked in yellow in Fig. 3(a)]. When the frequency of 2.48 GHz is considered, the pseudospin-up component from the source can be filtered out and routed upleftward along the ΓK direction, while the pseudospin-down component is transferred along the $\Gamma K'$ direction. Such valley-dependent pseudospin-flow behavior is well demonstrated in Fig. 3(d) where the PD between E_z and H_z at $z = 3d_0/4$ is plotted. Obviously, the PD is stable around the value of 0 (cyan) at the end of the ΓK propagating channel. Such in-phase feature indicates that a nearly pure pseudospin-up state propagates along the ΓK direction. On the contrary, the propagating waves along the $\Gamma K'$ direction are pseudospin-down polarized as the PD is around π (red). On the other hand, as shown in Fig. 3(e), the pseudospin-down (pseudospin-up) state will be obtained at the end of the ΓK ($\Gamma K'$) propagating channel when the frequency of 2.92 GHz is considered. This PD distribution is distinct from that shown in Fig. 3(d). With the comparison between Figs. 3(d) and 3(e), reconfigurable PVHE is achieved by shifting the operating frequency in the same metacrystal waveguide. This frequency-direction locking phenomenon, which is originated from the unique four-band model with two monopolar and two dipolar modes, proves that a metacrystal waveguide is an excellent platform for not only observing pseudospin flow but also controlling it.

C. Pseudospin-direction locking propagation

The pseudospin-direction locking propagation is also identified in Fig. 4. We consider the metacrystal waveguide in domain I, e.g., that marked by the green dot in the phase diagram [Figs. 1 and 4(a)]. When an E_y-polarized face source (which is homogeneous along the z direction while having a Gaussian width of 300 mm along the y direction) is launched along the $+x$ direction, only pseudospin-down states propagating along the ΓK direction can be excited if the frequency of 2.9 GHz is considered. Figure 4(b) shows the E_z fields of rightward propagating pseudospin state at $z = 3d_0/4$. The E_z fields are parallel to the y axis at the right exit. As only the pseudospin-down component of the incident source is filtered and transferred rightward, the PD is stable around π [red in Fig. 4(c)]. In contrast, when the source is placed on the right, the pseudospin-up state propagating leftward along the $\Gamma K'$ direction is excited [Fig. 4(d)]. This is verified by the result shown in Fig. 4(e) where the PD is stable around 0 (cyan) at the left exit of the metacrystal waveguide.

Pseudospin-direction locking propagation is unique in inversion asymmetric metacrystal waveguides. As a comparative case, we study the transmission in an inversion symmetric metacrystal waveguide in Fig. 5. As shown in Fig. 5(a), we consider the metacrystal waveguide whose band structure has been presented in Fig. 2(c). As the inversion symmetry is

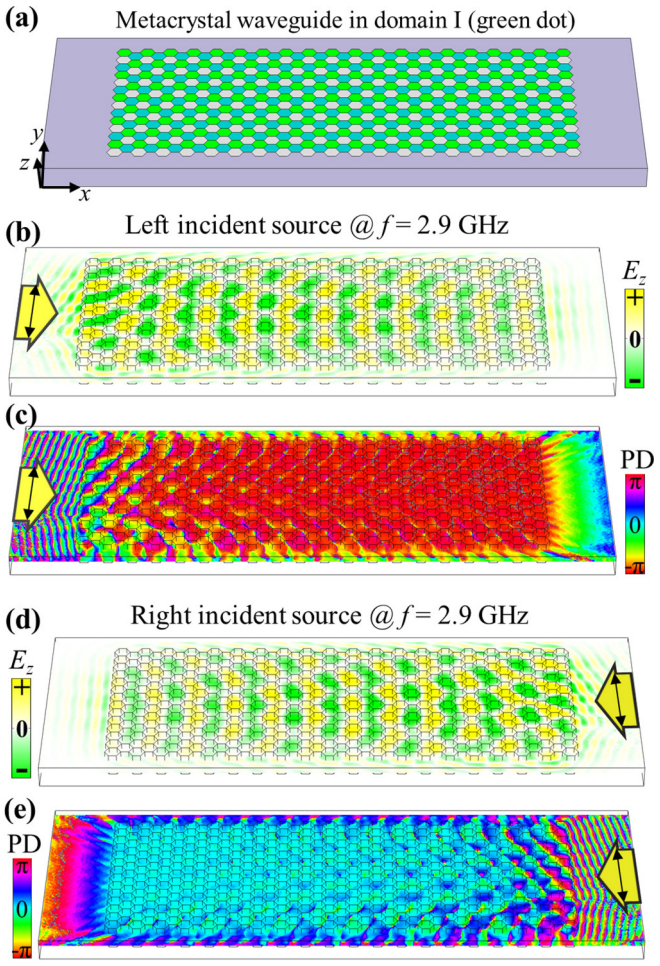

FIG. 4. Pseudospin-direction locking propagation in bulk metacrystal waveguide. (a) Schematic of the metacrystal waveguide which has been illustrated in Fig. 1 and marked by the green dot in the phase diagram in Fig. 2. An E_y-polarized source is launched along the $+x$ or $-x$ direction, with the operating frequency of $f = 2.9$ GHz. (b), (c) When the source is launched on the left, only the rightward pseudospin-down state propagating along the ΓK direction is excited, and the PD is around π (red). (d), (e) On the contrary, when the source is incident on the right, the leftward propagating pseudospin-up state along the $\Gamma K'$ direction is excited, and the PD is almost 0 (cyan).

kept, pseudospin-up and pseudospin-down states are doubly degenerate. Hence an E_y incident source launching on the right will excite both leftward pseudospin-up and pseudospin-down flow. These two pseudospin states interfere with each other when they propagate along the bulk crystal, resulting in the nonparallel output E_z fields. This is demonstrated by the wavefront distortion at the left exit in Fig. 5(b). As no pure pseudospin flow is obtained at the left exit, the PD distributions are messy and dependent on the y positions.

D. Prototype of photonic blocker

The valley-dependent pseudospin-split bulk band and the associated valley DOF open a route toward the discovery of alternative states of light and fancy applications such as pseudospin-dependent light propagation and nonreciprocal

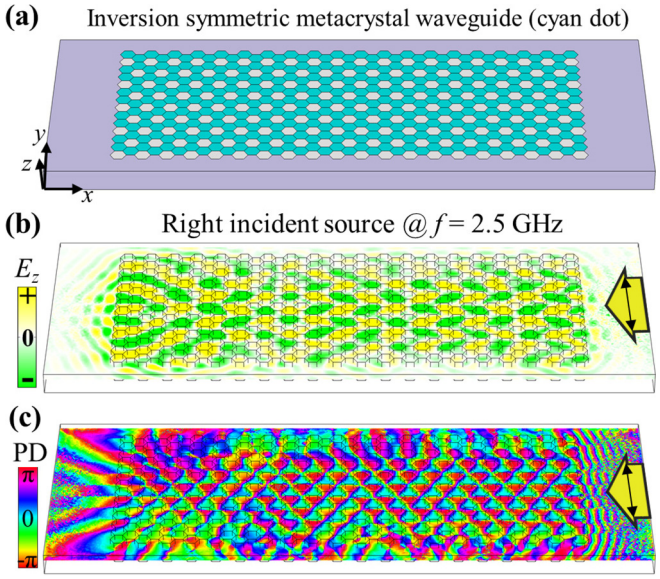

FIG. 5. Absence of pseudospin-direction locking propagation in the inversion symmetric metacrystal waveguide. (a) Schematic of the inversion symmetric metacrystal waveguide as that shown in Fig. 2(c). (b) Nonparallel output E_z fields and (c) messy PD distributions at the left exit when an E_y-polarized source is incident on the right, with the frequency of $f = 2.5$ GHz. This is because both pseudospin-up and pseudospin-down states are excited, and they interfere with each other while propagating along the bulk crystal.

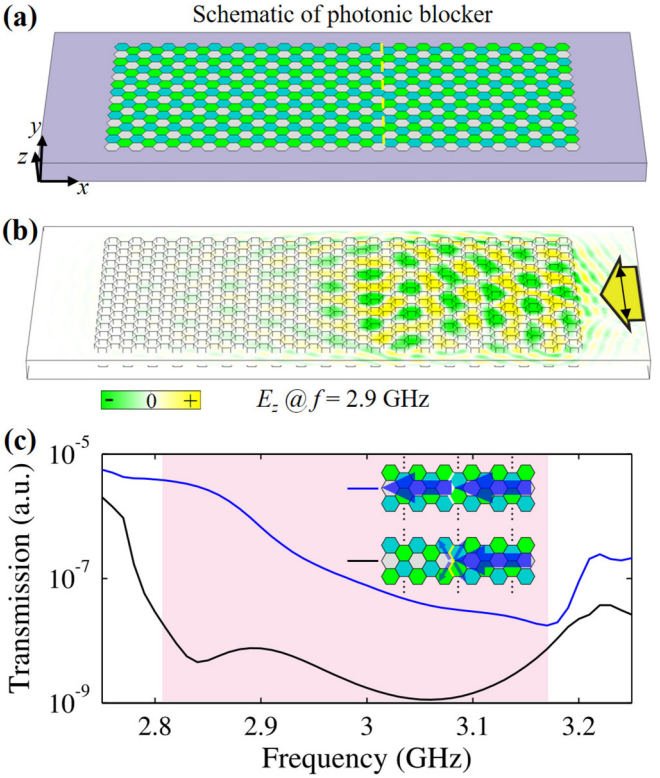

FIG. 6. Prototype of photonic blocker. (a) Schematic of photonic blocker which is constructed by cascading two metacrystal waveguides together. (b) The E_z fields for photonic blocker at the frequency of 2.9 GHz. Low transmittance is observed in the left exit of the propagating channel. (c) Transmittance spectra for no-blocker (blue) and photonic blocker (black). For the nonblocker, the leftward pseudospin-up flow meets no obstacles (top inset) while the excited pseudospin-up flow is reflected and refracted at the interface (bottom inset). Hence, the transmittance of the photonic blocker case is two orders of magnitude lower than that of the nonblocker.

transport of pseudospin states. In this section, we show the prototype of a photonic blocker which is constructed by cascading two metacrystal waveguides [Fig. 6(a)]. The metacrystal waveguide locating on the right of the dashed yellow line is that presented in Figs. 1 and 3(a), while the metacrystal waveguide on the left is obtained by inverting the right one by 180° along the z direction. When the incident source is placed on the right, it excites leftward pseudospin-up flow along the first metacrystal waveguide [see in Figs. 4(d) and 4(e)]. However, as the left metacrystal waveguide only supports leftward pseudospin-down flow, the excited pseudospin-up flow in the right metacrystal waveguide will be reflected and refracted at the interface [see the bottom inset in Fig. 6(c)]. Hence, low transmittance will be observed at the left exit and the photonic blocker can be realized. To test the performance of this proposed photonic blocker, we do the transmission simulation. As presented in Fig. 6(b), the excited light flow by the right incident source is strongly reflected or refracted, and it leads to the enhanced E_z fields at the right-hand side. Nearly zero fields are observed at the left-hand side of this blocker. We also calculate the transmittance of the photonic blocker and study the no-blocker case [i.e., Fig. 4(c)] for comparison. The transmittance of the photonic blocker case is two orders of magnitude lower than that of the nonblocker case [Fig. 6(c)].

E. Experimental design of metacrystal waveguide

In this section, we will present a concrete design for the proposed 3D metacrystal waveguide. As stated above, the 3D metacrystal waveguide consists of two parallel metal plates at $z = 0$ mm and $z = 48$ mm, and one sandwiched metacrystal with a height of 48 mm. As shown in Fig. 7(a), the designed metacrystal consists of six layers of metamaterials along the z direction. Each single layer has a height of 8 mm, and it consists of one acrylic glass plate on the bottom, one array of meta-atoms in the middle, and another acrylic glass plate on the top [Fig. 7(b)]. The acrylic glass plates have a height of 3 mm, and they are drilled with a honeycomb lattice (lattice constant of 30 mm) of through holes (diameter of 12 mm). To place the meta-atom array, blind holes with a height of 2.1 mm should also be drilled at the unit-cell center of the predrilled honeycomb through holes. The geometries of these blind holes depend on the geometries of meta-atoms that are placed on them. Between two acrylic glass plates, meta-atoms with "gyro" or "star" geometries are placed [Fig. 7(c)]. As shown in the top panel of Fig. 7(c), the gyro meta-atom consists of two concentric metallic cylinders with different diameters and heights, i.e., the "fat-short" cylinder with ($d_1 = 26.8$ mm, $h_1 = 1$ mm) and the "thin-tall" cylinder with ($d_2 = 5.4$ mm, $h_2 = 6.2$ mm). The star meta-atom is constructed by three identical metallic blocks each rotated 60° with respect to one another. The size of each metallic block is 18.7 mm × 4.6 mm × 6.2 mm [bottom panel of Fig. 7(c)]. With these well-designed

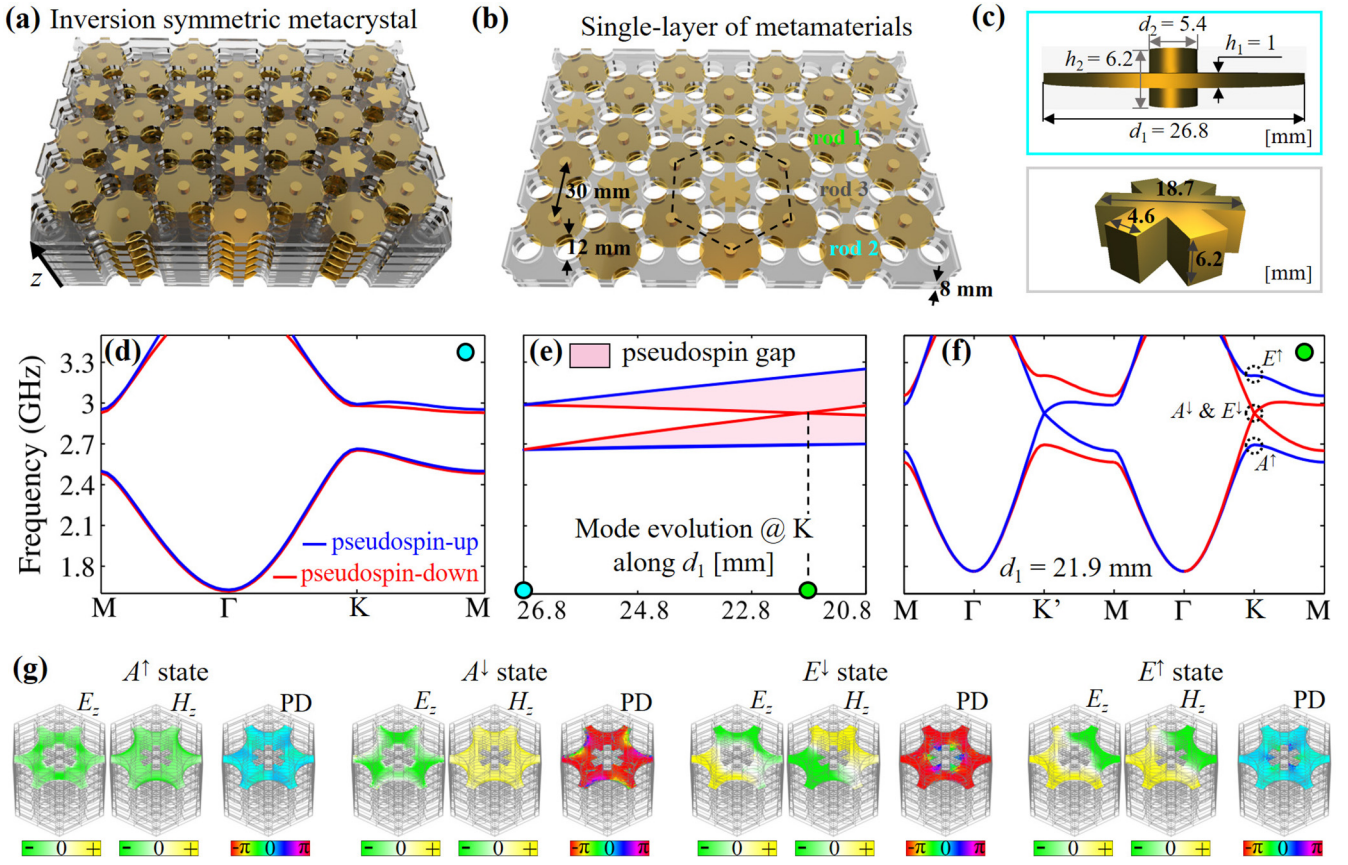

FIG. 7. Experimental design and band structure of the realistic metacrystal waveguide. (a) Schematic of the inversion symmetric metacrystal consisting of six layers of metamaterials which are stacked along the z direction. (b) Schematic of one single layer of metamaterials with a height of 8 mm. It consists of two acrylic glass plates with drilled holes and one array of meta-atoms. The unit cell of the meta-atom array consists of one star meta-atom surrounded by two gyro meta-atoms (dashed black hexagon). In accordance with the conceptual structure proposed in Figs. 1 and 2, the rod 1, rod 2, and rod 3 regions are labeled. (c) Schematics and structural parameters for the gyro (top panel) and star (bottom panel) meta-atoms. (d) Pseudospin degenerate band structure for inversion symmetric metacrystal waveguide with $d_1 = 26.8$ mm. (e) Frequency spectra of four pseudospin states at the K point as a function of the diameter of the short-fat cylinder (d_1) in the gyro meta-atoms located in rod 1 region. (f) Valley-dependent pseudospin-split band structure for metacrystal waveguide with $d_1 = 21.9$ mm. All bands are marked in blue (pseudospin-up) or red (pseudospin-down) according to the pseudospin polarizations of the eigenstates on them. Frequency isolated pseudospin-split bulk bands appear near the K' and K valleys. (g) Eigenfields of four pseudospin states at the K point, sharing the same irreducible representations and pseudospin notations as those in Fig. 1(c).

gyro and star meta-atoms, we construct the unit cell of the meta-atom array by surrounding one star meta-atom with two gyro meta-atoms [outlined by the dashed black hexagon in Fig. 7(b)].

In short, to construct the realistic 3D metacrystal waveguide, we first array the meta-atoms, and sandwich them between two acrylic glass plates to form one single layer of metamaterials, then stack six layers of metamaterials along the z direction, and lastly put two metal plates at $z = 0$ and $z = 48$ mm. Figure 7(d) shows the corresponding band structure of this inversion symmetric metacrystal waveguide. Protected by both the time-reversal and inversion symmetries, pseudospin states are doubly degenerate in the whole Brillouin zone. To break the inversion symmetry, we reduce the diameter of the short-fat cylinder (d_1) in the gyro meta-atoms located in the rod 1 region [labeled in green in Fig. 7(b)]. Frequency spectra of the four pseudospin states at the K point as a function of d_1 are shown in Fig. 7(e). At $d_1 = 26.8$ mm (marked by the cyan dot), the $A^{\uparrow}$ and $A^{\downarrow}$ ($E^{\uparrow}$ and $E^{\downarrow}$) states are frequency degenerate as the inversion symmetry is preserved. Particularly, two pseudospin-down states are accidentally degenerate when $d_1 = 21.9$ mm (marked by the green dot). The bandwidth of the pseudospin gap is enlarged. Hence, the metacrystal waveguide with $d_1 = 21.9$ mm is chosen and its band structure is shown in Fig. 7(f). Similar to the band structure of the metacrystal waveguide with effective parameters presented in Fig. 1(b), bands along the ΓM direction are nearly degenerate but pseudospin-split bulk bands are found near the K' and K valleys. Although pseudospin states at the M point are not exactly degenerate, it would not affect the valley-controlled propagation of the pseudospin state as the related frequency region is far from the frequency range of interest. In addition, we also plot out the eigenfields at $z = 3d_0/4$ of four pseudospin states at the K point. Both the irreducible representation and pseudospin polarization of each pseudospin state are in good agreement with the theoretical results in Fig. 1(c). From the band structure and the eigenfields in Fig. 7, we expect that the above-mentioned valley-controlled behaviors, such as reconfigurable PVHE, pseudospin-direction

locking propagation, and photonic blocker, can be experimentally observed in this designed metacrystal waveguide around 3 GHz.

IV. CONCLUSION

In conclusion, we discuss the valley-controlled propagation of pseudospin states in 3D bulk metacrystal waveguides without Dirac cones. Valley-dependent pseudospin bands and the phase diagram of pseudospin states are obtained in metacrystal waveguides by breaking the inversion symmetry and changing the constitutive parameters. With the phase diagram, frequency-direction locking pseudospin flow, i.e., reconfigurable PVHE, is achieved by shifting the working frequency. Pseudospin-direction locking propagation is also realized by using the valley DOF. Employing the pseudospin-filtered feature of inversion asymmetric metacrystal waveguides, we further demonstrate a prototype of a photonic blocker. Lastly, a realistic metamaterials design of the proposed 3D metacrystal waveguides is discussed.

The metacrystal waveguide is a good platform for controlling pseudospin flow as it has many more structural parameters for design. For example, the proposal of reconfigurable photonic valley Hall effect benefits from the complete transition diagram of the metacrystal waveguide, resulting in frequency-direction locking behavior which is hardly achieved in previous photonic systems (e.g., Ref. [40]) and condensed-matter systems. Note that we focus on valley-controlled propagation of bulk states in the inversion-symmetry-breaking system in this work, while the topologically protected behavior such as robust transport of edge states has been observed in an inversion-symmetry-invariant metacrystal waveguide [23].

We would also like to note that valley-dependent electromagnetic wave behaviors can also be exploited by breaking the inversion symmetry in other photonic systems such as three-dimensional photonic crystals, silicon-based metamaterials, and gyrotropic media. It will pave a way to not only fundamental physics that is difficult to observe in electronic systems, but also the next generation of optical communication devices based on pseudospin-dependent light propagation, and nonreciprocal transport of pseudospin states.

ACKNOWLEDGMENTS

This work is supported by the Natural Science Foundation of China (Grants No. 11522437, No. 11704422, No. 61775243, and No. 11761161002), and Fundamental Research Funds for the Central Universities (Grant No. 17lgpy19).

[1] S.-Y. Lin, E. Chow, V. Hietala, P. R. Villeneuve, and J. D. Joannopoulos, Experimental demonstration of guiding and bending of electromagnetic waves in a photonic crystal, Science **282**, 274 (1988).

[2] H. Gersen, T. J. Karle, R. J. P. Engelen, W. Bogaerts, J. P. Korterik, N. F. van Hulst, T. F. Krauss, and L. Kuipers, Real-Space Observation of Ultraslow Light in Photonic Crystal Waveguides, Phys. Rev. Lett. **94**, 073903 (2005).

[3] G. Zheng, H. Mühlenbernd, M. Kenney, G. Li, T. Zentgraf, and S. Zhang, Metasurface holograms reaching 80% efficiency, Nat. Nanotechnol. **10**, 308 (2015).

[4] X. Ni, Z. J. Wong, M. Mrejen, Y. Wang, and X. Zhang, An ultrathin invisibility skin cloak for visible light, Science **349**, 1310 (2015).

[5] X. Xiong, Z.-H. Xue, C. Meng, S.-C. Jiang, Y.-H. Hu, R.-W. Peng, and M. Wang, Polarization-dependent perfect absorbers/reflectors based on a three-dimensional metamaterial, Phys. Rev. B **88**, 115105 (2013).

[6] Y. Shen, D. Ye, I. Celanovic, S. G. Johnson, J. D. Joannopoulos, and M. Soljačić, Optical broadband angular selectivity, Science **343**, 1499 (2014).

[7] N. Shitrit, I. Yulevich, E. Maguid, D. Ozeri, D. Veksler, V. Kleiner, and E. Hasman, Spin-optical metamaterial route to spin-controlled photonics, Science **340**, 724 (2013).

[8] J. Lin, J. P. B. Mueller, Q. Wang, G. Yuan, N. Antoniou, X.-C. Yuan, and F. Capasso, Polarization-controlled tunable directional coupling of surface plasmon polaritons, Science **340**, 331 (2013).

[9] F. J. Rodriguez-Fortuno, G. Marino, P. Ginzburg, D. O'Connor, A. Martinez, G. A. Wurtz, and A. V. Zayats, Near-field interference for the unidirectional excitation of electromagnetic guided modes, Science **340**, 328 (2013).

[10] M. Burresi, R. J. P. Engelen, A. Opheij, D. van Oosten, D. Mori, T. Baba, and L. Kuipers, Observation of Polarization Singularities at the Nanoscale, Phys. Rev. Lett. **102**, 033902 (2009).

[11] I. Söllner, S. Mahmoodian, S. L. Hansen, L. Midolo, A. Javadi, G. Kiršanskė, T. Pregnolato, H. El-Ella, E. H. Lee, J. D. Song, S. Stobbe, and P. Lodahl, Deterministic photon-emitter coupling in chiral photonic circuits, Nature Nanotechnol. **10**, 775 (2015).

[12] J. Petersen, J. Volz, and A. Rauschenbeutel, Chiral nanophotonic waveguide interface based on spin-orbit interaction of light, Science **346**, 67 (2014).

[13] R. Mitsch, C. Sayrin, B. Albrecht, P. Schneeweiss, and A. Rauschenbeutel, Quantum state-controlled directional spontaneous emission of photons into a nanophotonic waveguide, Nat. Commun. **5**, 5713 (2014).

[14] L. Lu, J. D. Joannopoulos, and M. Soljačić, Topological photonics, Nat. Photonics **8**, 821 (2014).

[15] C. He, L. Lin, X.-C. Sun, X.-P. Liu, M.-H. Lu, and Y.-F. Chen, Topological photonic states, Int. J. Mod. Phys. B **28**, 1441001 (2013).

[16] S. A. Skirlo, L. Lu, and M. Soljačić, Multimode One-Way Waveguides of Large Chern Numbers, Phys. Rev. Lett. **113**, 113904 (2014).

[17] K. Fang, Z. Yu, and S. Fan, Realizing effective magnetic field for photons by controlling the phase of dynamic modulation, Nat. Photonics **6**, 782 (2012).

[18] M. C. Rechtsman, J. M. Zeuner, Y. Plotnik, Y. Lumer, D. Podolsky, F. Dreisow, S. Nolte, M. Segev, and A. Szameit, Photonic Floquet topological insulators, Nature **496**, 196 (2013).

[19] Y. Hatsugai, Chern Number and Edge States in the Integer Quantum Hall Effect, Phys. Rev. Lett. **71**, 3697 (1993).

[20] A. B. Khanikaev, S. H. Mousavi, W.-K. Tse, M. Kargarian, A. H. MacDonald, and G. Shvets, Photonic topological insulators, Nat. Mater. **12**, 233 (2012).

[21] M. Hafezi, E. A. Demler, M. D. Lukin, and J. M. Taylor, Robust optical delay lines with topological protection, Nat. Phys. **7**, 907 (2011).

[22] L.-H. Wu and X. Hu, Scheme for Achieving a Topological Photonic Crystal by Using Dielectric Material, Phys. Rev. Lett. **114**, 223901 (2015).

[23] W.-J. Chen, S.-J. Jiang, X.-D. Chen, B. Zhu, L. Zhou, J.-W. Dong, and C. T. Chan, Experimental realization of photonic topological insulator in a uniaxial metacrystal waveguide, Nat. Commun. **5**, 5782 (2014).

[24] X. Cheng, C. Jouvaud, X. Ni, S. H. Mousavi, A. Z. Genack, and A. B. Khanikaev, Robust reconfigurable electromagnetic pathways within a photonic topological insulator, Nat. Mater. **15**, 542 (2016).

[25] B. Xiao, K. Lai, Y. Yu, T. Ma, G. Shvets, and S. M. Anlage, Exciting reflectionless unidirectional edge modes in a reciprocal photonic topological insulator medium, Phys. Rev. B **94**, 195427 (2016).

[26] K. Lai, T. Ma, X. Bo, S. Anlage, and G. Shvets, Experimental realization of a reflections-free compact delay line based on a photonic topological insulator, Sci. Rep. **6**, 28453 (2016).

[27] D. Xiao, W. Yao, and Q. Niu, Valley-Contrasting Physics in Graphene: Magnetic Moment and Topological Transport, Phys. Rev. Lett. **99**, 236809 (2007).

[28] A. Rycerz, J. Tworzydło, and C. W. J. Beenakker, Valley filter and valley valve in graphene, Nat. Phys. **3**, 172 (2007).

[29] H. Pan, Z. Li, C.-C. Liu, G. Zhu, Z. Qiao, and Y. Yao, Valley-Polarized Quantum Anomalous Hall Effect in Silicene, Phys. Rev. Lett. **112**, 106802 (2014).

[30] X. Xu, W. Yao, D. Xiao, and T. F. Heinz, Spin and pseudospins in layered transition metal dichalcogenides, Nat. Phys. **10**, 343 (2014).

[31] X. Wu, Y. Meng, J. Tian, Y. Huang, H. Xiang, D. Han, and W. Wen, Direct observation of valley-polarized topological edge states in designer surface plasmon crystals, Nat. Commun. **8**, 1304 (2017).

[32] T. Ma and G. Shvets, All-Si valley-Hall photonic topological insulator, New J. Phys. **18**, 025012 (2016).

[33] X.-D. Chen, F.-L. Zhao, M. Chen, and J.-W. Dong, Valley-contrasting physics in all-dielectric photonic crystals: Orbital angular momentum and topological propagation, Phys. Rev. B **96**, 020202(R) (2017).

[34] R. K. Pal and M. Ruzzene, Edge waves in plates with resonators: An elastic analogue of the quantum valley Hall effect, New J. Phys. **19**, 025001 (2017).

[35] O. Bleu, D. D. Solnyshkov, and G. Malpuech, Quantum valley Hall effect and perfect valley filter based on photonic analogs of transitional metal dichalcogenides, Phys. Rev. B **95**, 235431 (2017).

[36] J. Noh, S. Huang, K. Chen, and M. C. Rechtsman, Observation of Photonic Topological Valley Hall Edge States, Phys. Rev. Lett. **120**, 063902 (2018).

[37] F. Gao, H. Xue, Z. Yang, K. Lai, Y. Yu, X. Lin, Y. Chong, G. Shvets, and B. Zhang, Topologically protected refraction of robust kink states in valley photonic crystals, Nat. Phys. **14**, 140 (2018).

[38] J. Lu, C. Qiu, M. Ke, and Z. Liu, Valley Vortex States in Sonic Crystals, Phys. Rev. Lett. **116**, 093901 (2016).

[39] J. Lu, C. Qiu, L. Ye, X. Fan, M. Ke, F. Zhang, and Z. Liu, Observation of topological valley transport of sound in sonic crystals, Nat. Phys. **13**, 369 (2016).

[40] J.-W. Dong, X.-D. Chen, H. Zhu, Y. Wang, and X. Zhang, Valley photonic crystals for control of spin and topology, Nat. Mater. **16**, 298 (2017).

[41] X.-D. Chen, Z.-L. Deng, W.-J. Chen, J.-R. Wang, and J.-W. Dong, Manipulating pseudospin-polarized state of light in dispersion-immune photonic topological metacrystals, Phys. Rev. B **92**, 014210 (2015).

[42] K. Sakoda, *Optical Properties of Photonic Crystals* (Springer Science & Business Media, New York, 2005).